An Active Turbulence Generator based on the Vortex Method for Simulation of a Complex Aerodynamic Admittance for Bridge Decks

Kavrakov, Igor*[1)], Argentini, Tommaso[2)], Omarini, Simone[2)], Rocchi, Daniele[2)], Morgenthal, Guido[1)]

1) Bauhaus-University Weimar, Weimar, Germany
2) Politecnico di Milano, Milan, Italy
**) presenting author, igor.kavrakov@uni-weimar.de*

ABSTRACT

The accurate description of the aerodynamic forces due to free-stream turbulence acting on a stationary bridge deck represents a challenging task. This paper presents a numerical approach based on the vortex particle method for the simulation of a two-dimensional complex aerodynamic admittance. Wakes of two fictitious airfoils are replicated by releasing vortex particles in a computational domain. The two airfoils constitute an active turbulence generator and when they oscillate harmonically in-phase, a sinusoidal vertical gust is generated along the centerline. A previously developed analytical model is extended in order to correlate the amplitude of the sinusoidal gust and the introduced circulation carried by the released vortex particles. The resulting aerodynamic forces of a section positioned downstream of the particle release locations are sinusoids, depending on the incoming gust frequency. The aerodynamic admittance is then determined as a transfer function between the aerodynamic forces and the incoming wind fluctuations. A verification of the method is first performed with the complex Sears' admittance for a flat plate. Finally, the numerical aerodynamic admittance for a streamlined bridge deck is validated with experimental results.

1 INTRODUCTION

The effect of the freestream turbulence on the bluff bodies is perplexing and not yet fully understood. A number of semi-analytical models have been developed throughout the years to model the aerodynamic forces due to wind gusts, which are commonly referred to as buffeting forces. In the linear unsteady model for aerodynamic forces acting a bridge deck, the buffeting forces are described as functions of the quasi-steady solution and frequency-dependent aerodynamic admittance. The latter represents a transfer function between the incoming harmonic gusts and aerodynamic forces. The concept of aerodynamic admittance in the linear unsteady model is based on fundamental two-dimensional (2D) linear airfoil theory developed by Sears (1936). Therein, the frequency-dependent deficiency of the aerodynamic forces for an incoming sinusoidal gust is introduced by the complex Sears' aerodynamic admittance function.

One of the experimental methods for determination of the aerodynamic admittance in its complex form is by using an active turbulence generator (ATG) (cf. Diana et al. (2003) and Diana et al. (2015)). An ATG represents a set of flapping airfoils, which generate sinusoidal gusts. The gusts generated in such way are assumed to be fully correlated in the span-wise direction, which comply with the 2D theory. By positioning a section downstream of the ATG, the aerodynamic admittance could be obtained for a particular frequency of oscillation of the airfoils.

The aerodynamic admittance function has been rarely determined by using numerical methods based on Computational Fluid Dynamics (CFD). In this paper, we introduce an alternative CFD method for the determination of the complex aerodynamic admittance, based on the Vortex Particle Method (VPM). An incoming sinusoidal gust is generated by modeling the wakes of two fictitious airfoils, positioned upstream of the section. In fact, the two fictitious airfoils constitute an ATG; hence, the method can be easily related to experiments. The article is organized as follows: The concept of aerodynamic admittance for bridge deck is briefly outlined in Sec. 2. In Sec. 3, we present the concept of an ATG for generating sinusoidal gusts in the VPM. Section 4 presents a brief study on the flow field. In Sec. 5, the aerodynamic admittance, obtained using the presented CFD method, is initially verified with the Sears' admittance for a flat plate, followed by experimental validation for a streamlined deck. Finally, concluding remarks are given in Sec. 6.

2 CONCEPT OF AERODYNAMIC ADMITTANCE

In the linear unsteady model, the aerodynamic admittance is defined as a transfer function between an incoming sinusoidal gust and the corresponding fluctuating aerodynamic forces acting on a section (cf. Fig. 1). The aerodynamic lift L and moment M forces acting on a body are given as follows (cf. e.g. Kavrakov and Morgenthal (2017)):

$$L(s) = \frac{1}{2}\rho U^2 B\left[C_L + 2C_L\chi_{Lu}(K)\frac{u(s)}{U} + (C_L' + C_D)\chi_{Lw}(K)\frac{w(s)}{U}\right], \tag{1}$$

$$M(s) = \frac{1}{2}\rho U^2 B^2\left[C_M + 2C_M\chi_{Mu}(K)\frac{u(s)}{U} + C_M'\chi_{Mw}(K)\frac{w(s)}{U}\right], \tag{2}$$

where ρ is the fluid density; U is the mean wind speed; u and w are the lateral and vertical wind fluctuations, respectively, and B is the body width. The lift, drag and moment static wind coefficients are denoted as C_D, C_L and C_M, respectively, and their derivative with respect to the mean angle of attack α_s is denoted with the prime notation. The reduced time is defined as $s = tU/B$, where t is the dimensional time. The aerodynamic admittance function χ_{jk} denote a transfer function between the force $j \in (L, M)$ due to incoming gust $k \in (u, w)$. In this work, we are mainly concerned with the aerodynamic admittance due to the vertical gust; hence, they can be obtained as follows (cf. Diana et al. (2003)):

$$\chi_{Lw}(K) = \frac{\mathcal{F}\left[L(t)-\overline{L(s)}\right]}{\frac{1}{2}\rho UB\,(C_L'+C_D)\mathcal{F}[w(s)]},\ \chi_{Mw}(K) = \frac{\mathcal{F}\left[M(s)-\overline{M(s)}\right]}{\frac{1}{2}\rho UB^2 C_M'\,\mathcal{F}[w(s)]}, \tag{3}$$

where the overbar denotes the mean value and $\mathcal{F}[\cdot]$ is the Fourier transform. The aerodynamic admittance functions concerning the longitudinal fluctuations, χ_{Lu} and χ_{Mu}, can be obtained in a similar manner as in Eq. (3). Since both, the aerodynamic forces and wind fluctuations are real signals, the aerodynamic admittance functions are complex functions of $K = \omega B/U$ (or $V_r = 2\pi/K$), for ω being the gust circular frequency (cf. Kavrakov and Morgenthal (2017)).

3 ACTIVE TURBULENCE GENERATOR BASED ON THE VORTEX METHOD

3.1 Concept

The concept of the present method is depicted in Fig. 1. Two fictitious airfoils (foil *FA* and foil *FB*), which constitute an fictitious ATG, are assumed to be oscillating upstream of the section. Their wake is modelled in a CFD domain by introducing particles carrying concentrated circulation $\Gamma_{F,j}^{in}$. The particles are introduced at two location at a constant time interval $\Delta t_F = m\Delta t$, where m is the particle release factor and Δt is the simulation time step. In case the oscillation of the airfoil is sinusoidal, the particles circulation is also sinusoidal, that is $\Gamma_F^{in}(t) =$

$\Gamma_{F0}^{in}(\Delta t_F)\, e^{i\omega t}$ and amplitude Γ_{F0}^{in} depends on the temporal (also spatial) discretization $\Delta t_F = \Delta x_F/U$, where $\Delta x_F$is the particle spacing. If both airfoils are oscillating in-phase, a sinusoidal gust is obtained along the center line, denoted as $w_c = w_{c0}e^{i\omega t}$, considering the planar wake assumption. The governing equations of the fluid in the CFD domain are numerically solved utilizing the VPM. Positioning a section downstream of the particle release locations, results in harmonic aerodynamic forces; hence, the aerodynamic admittance is easily computed (cf. Eq. (3)).

In light of the previous explanation, the presented method consists of two parts, in which: (i) the introduced circulation $\Gamma_F^{in}(t)$ is computed for prescribed gust amplitude w_{c0} and frequency; and (ii) a CFD simulation is performed considering the inflow (released) particles and a section. Therefore, two models are required for the two steps. For the first step, we utilize a semi-analytical and an inverse model for prediction of the circulation amplitude for a prescribed gust amplitude w_{ct0}. As noted previously, the VPM is utilized for the second step. It is noteworthy to notice, that the prescribed gust amplitude is utilized to only provide an approximate guess. This is to ensure up to a certain extent, that the aerodynamic forces are in the linear range for the determination of the aerodynamic admittance.

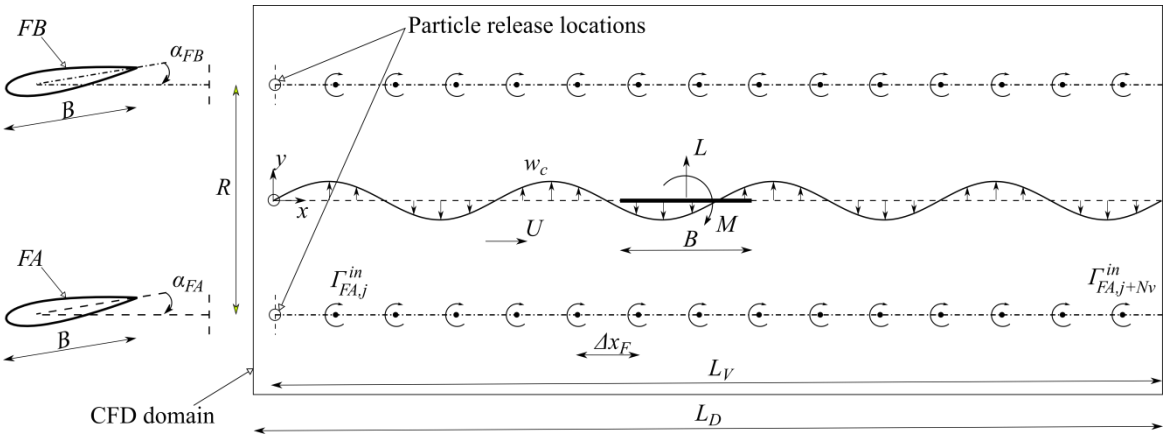

Figure 1: Concept for determination of the aerodynamic admittance based on a fictitious ATG.

3.2 Vortex Particle Method

First, we briefly outline the VPM to be able to easily correlate the discrete wakes of fictitious airfoils with the governing equations of the fluid. The vorticity transport equation of a viscous and homogeneous fluid in 2D is given as follows:

$$\frac{\partial \omega_u}{\partial t} + (\boldsymbol{u}\cdot\nabla)\omega_u = \nu\nabla^2\omega_u, \tag{6}$$

where ω_u is the vorticity, which is a scalar in 2D, ν is the kinematic viscosity and $\boldsymbol{u}$ is the velocity vector. The vorticity-velocity relation can be obtained by utilizing the Biot-Savart law as follows:

$$\boldsymbol{u}(\boldsymbol{x}) = \boldsymbol{U} - \frac{1}{2\pi}\int_{\mathcal{D}} \frac{(\boldsymbol{x}-\boldsymbol{y})\times\omega_u(\boldsymbol{y})}{|\boldsymbol{x}-\boldsymbol{y}|}\mathrm{d}\boldsymbol{y}, \tag{7}$$

The VPM method discretizes the vorticity field in a Lagrangian manner by particles, which are positioned at $\boldsymbol{x}_p$ and carry circulation Γ_p, as follows:

$$\boldsymbol{u}(\boldsymbol{x}_p) = \boldsymbol{U} - \sum_{p=1}^{N_P}\frac{\boldsymbol{e}_n\times(\boldsymbol{x}_p-\boldsymbol{x})}{|\boldsymbol{x}_p-\boldsymbol{x}|^2}\Gamma_p = \boldsymbol{U} - \sum_{p=1}^{N_P}\boldsymbol{K}(\boldsymbol{x}_p-\boldsymbol{x})\,\Gamma_p, \tag{8}$$

where $\boldsymbol{e}_n$ is a vector perpendicular to the fluid plane. In the VPM, the velocity kernel $\boldsymbol{K}$ is substituted by a mollified velocity kernel $\boldsymbol{K}_\epsilon$to account for the numerical instabilities. Herein, we use the two-step viscous splitting procedure to solve Eq. 6. In the first step, the kinetics are solved utilizing the fast P^{3}M algorithm of the Poisson equation obtained from Eq. 8, while the 4th order Runge-Kutta is utilized for the dynamics of the particles (cf. Morgenthal (2002)). In the second step, the viscosity is included by using the random walk method. It is important to note, that the additional constraint of the vorticity boundary conditions, that is, the Kelvin circulation's theorem, is modified to account for the released particles as $\sum\Gamma = \sum\Gamma_{\mathrm{F}}^{\mathrm{in}}$.

3.3 Analytical model for circulation amplitude prediction

The concept for generating sinusoidal gust using an ATG has been used previously in experiments (cf., e.g. Diana et al. (2003), Diana et al. (2015), Stapountzis (1982)), as noted in Sec. 1. In the case of experiments, the goal is to correlate the amplitude of oscillation of the airfoils, α_{FA0} and α_{FB0}, to the gust amplitude w_{c0} at a point along the center line at point $\boldsymbol{x}_c = (x, 0)$ (cf. Fig. 1). Stapountzis (1982) developed an analytical model to correlate the foil amplitude to the velocity amplitudes for sinusoidal gusts, while Harding and Bryden (2012) introduced an inverse numerical model for general velocity fluctuations. The latter is given in the next section, while the analytical model by Stapountzis (1982) is given herein and is extended to relate w_{c0} and Γ_{F0}^{in}. The analytical model is based on five assumptions, which are paraphrased herein as: (i) the airfoils are idealized as flat plates; (ii) the airfoil oscillation amplitudes are sufficiently small, so that linear unsteady theory applies; (iii) the vorticity shed from an airfoil into the wake is concentrated at the mean line and is convected by the mean velocity (planar wake assumption); (iv) the wakes are infinite, non-interfering and the point $\boldsymbol{x}_c$ is located sufficiently downstream that the bound circulation of the airfoils is negligible and (v) the Kutta-Jukowski condition is constantly fulfilled.

Taking the previous assumptions into account, the horizontal and vertical velocities at point $\boldsymbol{x}_c$ can be obtained by using the Biot-Savart law (cf. Eq. 7 and Fig.1) as follows:

$$u(\boldsymbol{x}_c, t) = u_c(t) = \frac{R}{4\pi}\int_{-\infty}^{\infty} \frac{\gamma_{FB}(x,t) - \gamma_{FB}(x,t)}{(x_c - x)^2 - R^2/4}\,\mathrm{d}x, \tag{9}$$

$$w(\boldsymbol{x}_c, t) = w_c(t) = \frac{-1}{2\pi}\int_{-\infty}^{\infty} \frac{(x_c - x)[\gamma_{FB}(x,t) + \gamma_{FB}(x,t)]}{(x_c - x)^2 - R^2/4}\,\mathrm{d}x, \tag{10}$$

where $\gamma_{FA} = \gamma_{FB} = \gamma_F$ is the circulation per unit length. For a sinusoidal oscillation of the airfoils, and thus sinusoidal γ_F, the integrals in Eqs. (9) and (10) are solved analytically by Stapountzis (1982) as a function of α_{F0}. In this work, we concentrate on the vertical fluctuating velocity on a point along the centerline for airfoils oscillating in-phase and therefor, the solution of Eq. (10) is given as follows (cf. Stapountzis (1982) for details):

$$w_c(t) = iF(k)e^{-\frac{kR}{B} + i(\omega t - 2kx/B)}, \tag{11}$$

where $k = \omega B/2U$, for ω being the oscillation frequency of the airfoil, $i = \sqrt{-1}$ and

$$F(k) = -4U\alpha_{F0}\frac{1 + (0.5 - 2l/B)ik}{H_1^{(2)}(k) + iH_0^{(2)}(k)}, \tag{12}$$

where $H_1^{(2)}$ and $H_0^{(2)}$ are Hankel functions of second kind and l represents the center of oscillation of the airfoils. The following equations are derived in order to relate Eqs. (11) and (12) to the circulation amplitude Γ_{F0}^{in} of the released particles, as explained in the Sec. 3.1.
We assume that the airfoils oscillate about the front quarter point; hence the center of oscillation

amounts to $l = -0.25B$. Rearranging Eqs. (11) and (10) for α_{F0} and using the non-dimensional time $s = tU/B$ the following expression is obtained:

$$\alpha_{F0} = \frac{w_c(s)\left[H_1^{(2)}(k)+iH_0^{(2)}(k)\right]}{-4U(1+ik)i} e^{\frac{kR}{B}-i(2ks-2kx/B)}. \tag{13}$$

For sinusoidal motion in-phase motion of airfoils, the vertical fluctuation is also a sinusoidal function, that is, $w_c(s) = w_{c0}e^{i2ks}$. Taking this into account and changing for $\alpha_F(s) = \alpha_{F0}e^{i2ks} = \alpha_e(s)/C(K)$, we obtain the following expression:

$$\frac{\alpha_e(s)}{C(k)} = \frac{w_{0c}\left[H_1^{(2)}(k)+iH_0^{(2)}(k)\right]}{4U(k-1i)} e^{\frac{kR}{B}-i(2ks-2kx/B)}, \tag{14}$$

where $\alpha_e(s)$ is the effective angle of attack, which takes into account the transient development of circulation and $C(k) = H_1^{(2)}(k)/[H_1^{(2)}(k) + iH_0^{(2)}(k)]$ is the Theodorsen's function. Changing for Theodorsen's function in Eq. (14) and using the Kutta-Jukowski theorem for the bound circulation, that is, $\Gamma_b(s) = UC_L'\alpha_e(s)B/2$, where $C_L' = 2\pi$, the following expression can be obtained:

$$\Gamma_b(s) = \frac{w_{c0}\pi B\, H_1^{(2)}(k)}{4(k-1i)} e^{\frac{kR}{B}+i2ks}. \tag{14}$$

In the preceding equation, the term $2kx/B$ is omitted as it only represents a constant phase between the airfoils and the fluctuation at position x. The vorticity shed in the wake due to change of angle of the airfoil during time $\Delta s_F = \Delta t_F U/B$ is $\Gamma_{FA}^{in}(s) = \Gamma_{FB}^{in}(s) = \Gamma_F^{in}(s) = \Gamma_b(s - \Delta s_F) - \Gamma_b(s)$. Since we assumed a continuous sinusoidal oscillation of the airfoils, the discrete circulation released into the domain yields the subsequent form:

$$\Gamma_{F,j}^{in} = \frac{w_{c0}\pi B\, H_1^{(2)}(k)}{4(k-1i)} e^{\frac{kR}{B}}\left(e^{-i2k\Delta s_F} - 1\right)e^{i2kj\Delta s_F}, \tag{15}$$

where $j = (1, \dots, \lfloor N_s/m \rfloor)$, for N_s being the number of simulation time-steps. The preceding equation can be written in the subsequent form $\Gamma_{F,j}^{in} = \Gamma_{F0}^{in}(\Delta s_F)\, e^{i2kj\Delta s_F}$. For specified gust frequency ω, gust amplitude w_{0c}, simulation time-step Δt, and seeding factor m, the computation of the column vector $\boldsymbol{\Gamma}_F^{in}$ is straight-forward. It is noted that the width of the fictitious airfoils in Eq. (15) is same as the width of the section to obtain a general non-dimensional form.

3.4 Inverse model for velocity amplitude prediction

Another way to obtain the vector containing the released circulation is by the inverse numerical model, which was introduced by Harding and Bryden (2012). The model makes use of the Biot-Savart law in a discrete form, given by Eq. (8). For the airfoil configuration depicted in Fig.1, the discrete velocities at point $\boldsymbol{x}_c$ are formulated as a discrete form of Eqs. (9) and (10) as follows:

$$\boldsymbol{u}_c = \boldsymbol{f} \cdot \left(\boldsymbol{\Gamma}_{FB}^{in} - \boldsymbol{\Gamma}_{FA}^{in}\right), \tag{16}$$

$$\boldsymbol{w}_c = \boldsymbol{g} \cdot \left(\boldsymbol{\Gamma}_{FA}^{in} + \boldsymbol{\Gamma}_{FB}^{in}\right), \tag{17}$$

where $\boldsymbol{u}_c$ and $\boldsymbol{w}_c$ are column vectors, with size $1 \times \lfloor N_s/m \rfloor$, of the discrete longitudinal and vertical velocities, respectively; $\boldsymbol{\Gamma}_{FB}^{in}$ and $\boldsymbol{\Gamma}_{FB}^{in}$ are column vectors with size $1 \times \lfloor N_s/m \rfloor + N_v$, where N_v are number of vortices considered in the spatial range of summation for the inverse model L_V^{inv}. The matrices $\boldsymbol{f}$ and $\boldsymbol{g}$ are of size $\lfloor N_s/m \rfloor \times \lfloor N_s/m \rfloor + N_v$ and practically represent the

velocity kernel $\boldsymbol{K}$ (cf. Sec. 3.2) for each component for the configuration in Fig. 1 (cf. Harding and Bryden (2012) for details). Equations (16) and (17) can be reversed and the released circulation vectors can be obtained as follows:

$$\boldsymbol{\Gamma}_{FA}^{in} - \boldsymbol{\Gamma}_{FB}^{in} = \boldsymbol{f}^{+}\boldsymbol{u}_c, \tag{18}$$

$$\boldsymbol{\Gamma}_{FA}^{in} + \boldsymbol{\Gamma}_{FB}^{in} = \boldsymbol{g}^{+}\boldsymbol{w}_c, \tag{19}$$

where the superscript "+" denotes the pseudo-inverse operation, as there is no unique inverse of $\boldsymbol{f}$ and $\boldsymbol{g}$ since the system is overdetermined. The pseudo-inverse is obtained by least-squares fit using the Moore-Penrose procedure. Equations (18) and (19) are solved as simulations equations.

The inverse model is given herein to verify the analytical model, described in the previous section (cf. Eq. (15)). Furthermore, it should be noted that $\boldsymbol{u}_c$ and $\boldsymbol{w}_c$ in Eqs. (16) and (17) apply for any prescribed fluctuations, not only for sinusoidal. Hence, the inverse model is more flexible than the analytical; however, numerical uncertainties might arise in the pseudo-inverse procedure and the selection of L_V^{inv}. It is noteworthy to mention that in case of periodic excitation, the spatial range of summation L_V^{inv} for the inverse model does not need to be the same length as L_V. By taking a larger L_V^{inv}, the numerical errors in the pseudo-inverse procedure can be avoided. However, these two lengths should be the same for arbitrarily prescribed fluctuations.

4 FLOW FIELD INVESTIGATION

In this section, we investigate the flow field without a section in the fluid domain by studying the quality and prediction amplitude of the incoming sinusoidal vertical gust.

A basic configuration is selected, using the following parameters: domain length $L_D/\mathrm{B} = 10$, vertical airfoil distance $R/B = 1$, target gust amplitude at the center line $w_{ct0}/U = 0.05$, Reynolds number (with respect to the fictitious airfoil width) $Re = 1 \times 10^4$, simulation time-step $\Delta s = 0.005$. The particle release factor m was chosen as such to accommodate either 30 vorticities per gust period or at least 200 vortices in the domain. With this condition, the particle release factor amounted to $12 \leq m \leq 21$, hence $0.060 \leq \Delta s_F \leq 0.105$ for the chosen reduced velocity range of $2 \leq V_r \leq 50$.

Figure 2 depicts a time history of the velocity fluctuations and their corresponding fast Fourier transforms (FFT) for a point on the center line at $x/B = 5$ and $V_r = 16$. A clear sinusoidal signal can be observed for both fluctuating components. The amplitude of the longitudinal fluctuations is an order of magnitude lower than the amplitude of the vertical fluctuations.

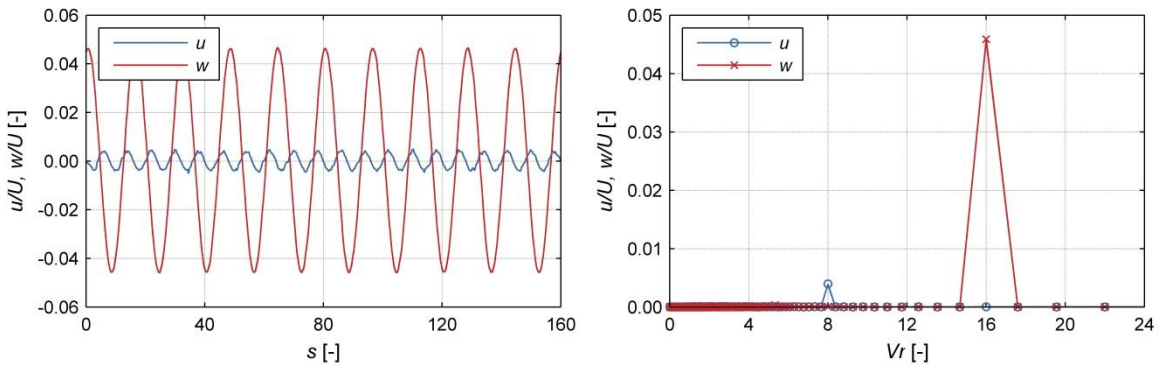

Figure 2: Time-histories of the velocity fluctuations (left) and their corresponding FFTs (right) at $V_r = 16$ and $x/B = 5$.

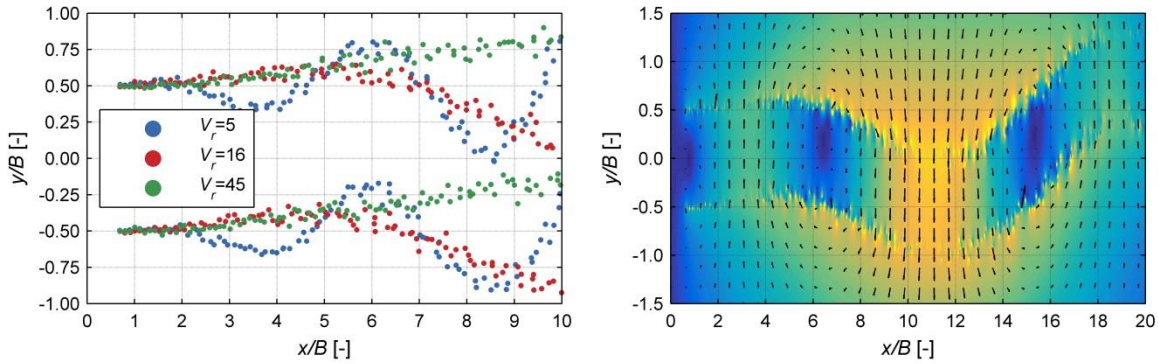

Figure 3: Instantaneous particle maps (left) and instantaneous velocity vector field at $V_r = 16$ (right).

Theoretically, for in-phase motion of the airfoils, there should be no longitudinal component. Furthermore, it can be observed that the vertical fluctuation amplitude is slightly underestimated. To further study the origin of these discrepancies in the CFD analyses, Figure 3 presents instantaneous particle maps within the domain three reduced velocities and an instantaneous velocity vector field at $V_r = 16$. It can be observed that the particles are not convected along a horizontal line. As expected, this discrepancy is more prominent for lower reduced velocities towards the particle release locations. Thus, the discrepancies in the amplitude of the vertical gust and the additional horizontal fluctuations are a consequence of the violation of planar wake (iii) and non-interference assumptions (iv) made in Sec. 3.3.

For the computation of the aerodynamic admittance it is important that the body is immersed in a uniform sinusoidal gust, while the gust amplitude is of minor significance as the aerodynamic forces are considered to be linear. In order to correctly position a section within the domain, it is of interest to study the gust uniformity and its harmonic component along the section width. Hence, we introduce a relative quality parameter Q, which quantifies the energy of a fluctuating velocity, concentrated at a single target frequency f_t, relative to the sum of the energy of the both fluctuating velocities. The quality parameter is defined as follows:

$$Q = \frac{S_w(f_t)}{\int_0^\infty [S_w(f)+S_u(f)]\mathrm{d}f}, \tag{20}$$

where S_u and S_w are the power spectral densities of the longitudinal and vertical fluctuations, respectively. The quality parameter Q and the ratio between the simulated and target gust amplitude w_{c0}/w_{ct0} at frequency f_t are the quantities of interest for the purpose in this work.

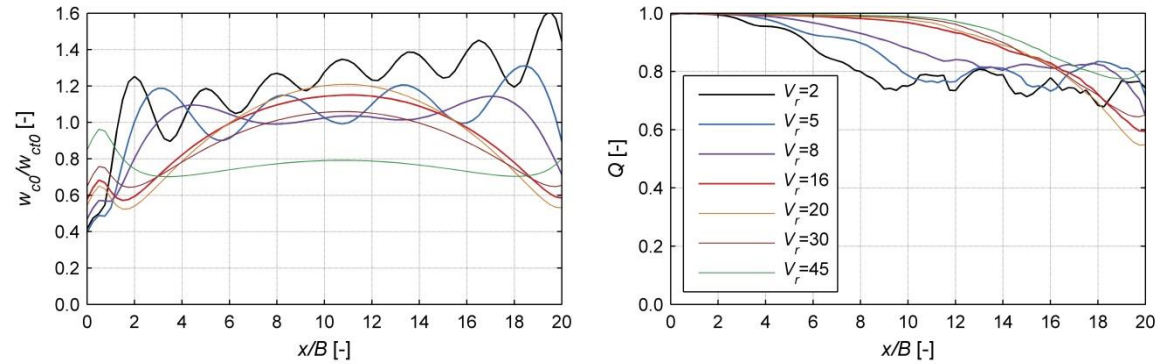

Figure 4: Influence of the reduced velocity on the relative gust amplitude (left) and quality parameter (right) along the center line.

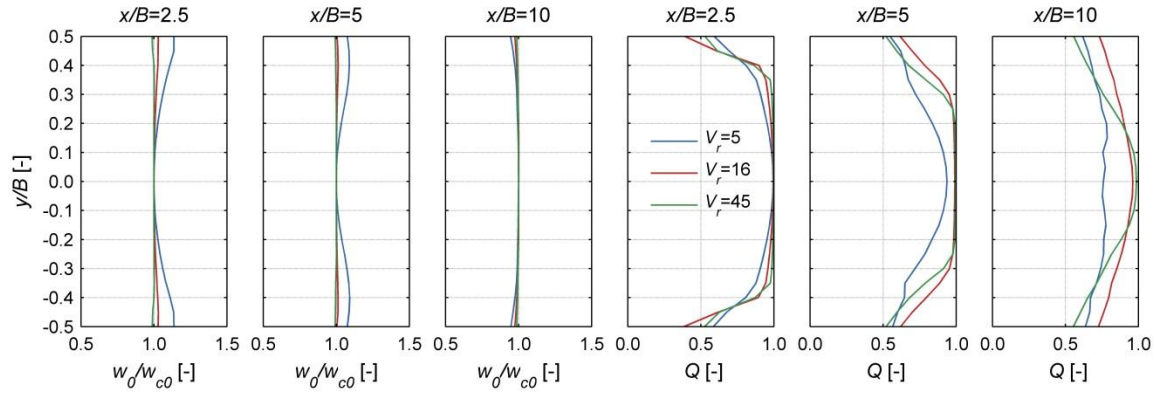

Figure 5: Influence of the reduced velocity on the relative gust amplitude (left) and quality parameter (right) between the particle-release locations.

Figure 4 and 5 depict the influence of the reduced velocity on flow quantities of interest along the center line and for three vertical profiles, respectively. After the particle release location, there is a certain length, in which the gust amplitudes converge (cf. Fig. 4, left). This convergence length increases with the increment of the reduced velocities, and it is approximately in the same range of magnitude as the gust length. Beyond this length, the gust amplitudes begin to "wobble", which is probably due to the distortion of the particle path (cf. Fig. 3, left). For gust lengths which are longer than half of the domain (i.e. $V_r \geq 15$), the convergence length is not reached and this behavior is not observed. The prediction of the magnitude of oscillation is within the $\pm 20\%$ range, taking the "wobbling" into account for most of the reduced velocities for $2 < x/B \leq 10$. In the case for the highest reduced velocity ($V_r = 45$), it can be observed that w_{c0} reached up to $0.8 w_{ct0}$. As noted previously, the quality parameter Q is more important for the aerodynamic admittance (cf. Fig. 4, right). It can be observed that the quality decays for points which are further downstream of the particle release locations. This decay occurs earlier for the lower reduced velocities, due to faster distortion of the path of released particles with respect to a horizontal path. Nevertheless, for a quality parameter more than 0.9, it can be assumed that the gust is considered as sinusoidal and most of the fluctuating energy is concentrated at a single vertical frequency.

The difference in amplitude along the height is appearing only for low reduced velocities, which are close to the particle release locations (cf. Fig. 5, left). However, this difference is relatively mild. Along the height, it can be observed that there is certain band with respect to the center line, for which the quality is relatively constant (cf. Fig. 6, right). This band reduces for vertical profiles, positioned further downstream of the particle release locations.

Figure 6 (left) depicts the amplitude of circulation in the wakes of the fictitious airfoils, obtained using the analytical model (cf. Sec. 3.3) and the inverse model by Harding and Bryden (2012) (cf. Sec. 3.4). The inverse model was computed for a summation length $L_V = 50B$, in order to minimize the numerical uncertainty. From the figure, it can be observed that the extension of the analytical model by Stapountzis (1982) (cf. Eq. 15) corresponds well with the inverse model. Furthermore, Stapountzis (1982) introduced a non-dimensional gust intensity to quantify the relation between the gust amplitude and oscillation amplitude of the airfoils as $I_g = w_0/U\alpha_{F0}$. In case of the analytical model, this relation is analytical. For the inverse model, the input variable is the w_0 and α_{F0} is computed, while for the CFD model the airfoil amplitude α_{F0} is the input variable (since it is analytically related to Γ_{F0}^{in}) and the gust intensity w_{c0} is the output variable. Figure 6 (right) depicts the non-dimensional gust intensity for the three models. For the CFD model, the point for the gust amplitude is the selected location where the section is positioned,

which is discussed in Sec. 5. Generally, good correspondence is obtained for the models, with some small discrepancies for very low reduced velocities and for gust lengths which are significantly longer than the domain length.

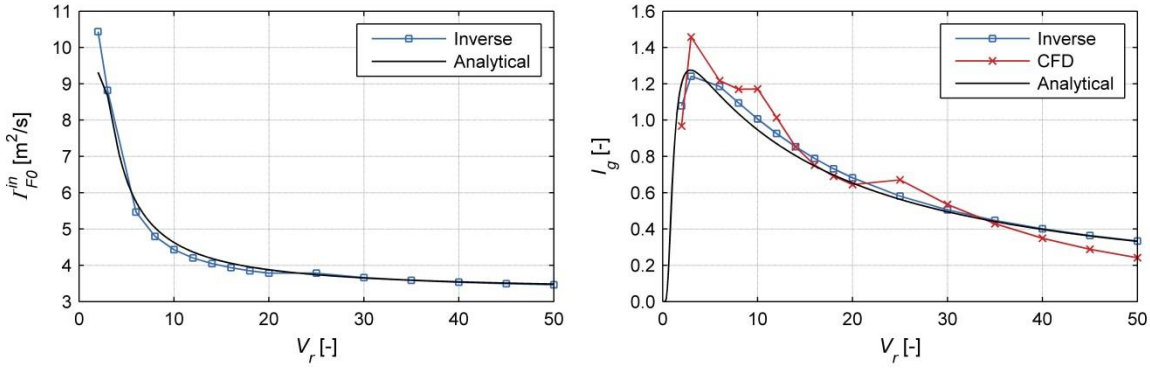

Figure 6: Amplitude of released circulation (left) and dimensionless gust intensity (right).

5 AERODYNAMIC ADMITTANCE – VERIFICATION AND VALIDATION

The main goal of this study is to evaluate the aerodynamic admittance for 2D immersed bodies subjected to sinusoidal gusts. In this section, initially we verify the method by computing Sears' admittance for a flat plate. This is followed by an experimental validation of the aerodynamic admittance for a streamlined bridge deck.

5.1 Analytical verification – flat plate

A rectangular section with width-to-depth ratio of 200 is introduced into the domain, in order to replicate a flat plate. The section is discretized on 400 panels. The Reynolds number is set as $Re = 1 \times 10^4$, for which the boundary layer is still not broken and the viscous effects are negligible. After the flow investigation (cf. Sec.4), it was decided that the stiffness centre of the flat plate is positioned at $x_c/B = 2$ for $V_r \leq 4$; $x_c/B = 5.5$ for $4 < V_r \leq 16$ and $x_c/B = 10$ for $V_r > 16$. The flow parameters and the domain is chosen as in Sec. 4. With this, a quality with gust is above 0.9 at the stiffness center and the released particles are not crossing the body.

The analytical aerodynamic admittance function, given by Sears (1941), is based on the linear theory and potential flow. Hence, the boundary layer and the static wind coefficients are verified for smooth freestream before subjecting the flat plate to sinusoidal gusts. Figure 7 (left) depicts the boundary layer with respect to the similarity parameter η for three locations along the flat plate, on the top and bottom side. Good correspondence with respect to the Blasius solution, can be observed and the symmetry of the flow is preserved. The lift and moment static wind coefficients with respect to the angle of attack α_s are given in Fig. 8 (right). These are further compared to their analytical counterparts, computed for lift and moment slopes of 2π and 0.5π, respectively. From the CFD analyses, the lift slope amounts to 1.924π and the moment slope amounts to 0.463π, resulting to 3.8% and 7.3% difference with respect to analytical counterparts. Next, the flat plate is subjected to sinusoidal gusts with reduced velocities ranging from $2 \leq V_r \leq 50$. Figure 8 depicts a sequence of particle maps for a cycle of sinusoidal gust past a flat plate at $V_r = 16$. It can be seen that even at the peak velocities (s=17.5 and s=25.5), the released particles do cross the body. To obtain the admittance, the sinusoidal gust needs to be tracked down at a specific location within the CFD domain. This can be conducted by two approaches: (i) track the sinusoidal gust at the location of the stiffness center from a separate simulation without a section the CFD domain and (ii) track the sinusoidal gust at a certain point upstream of the section in a CFD simulation including a section.

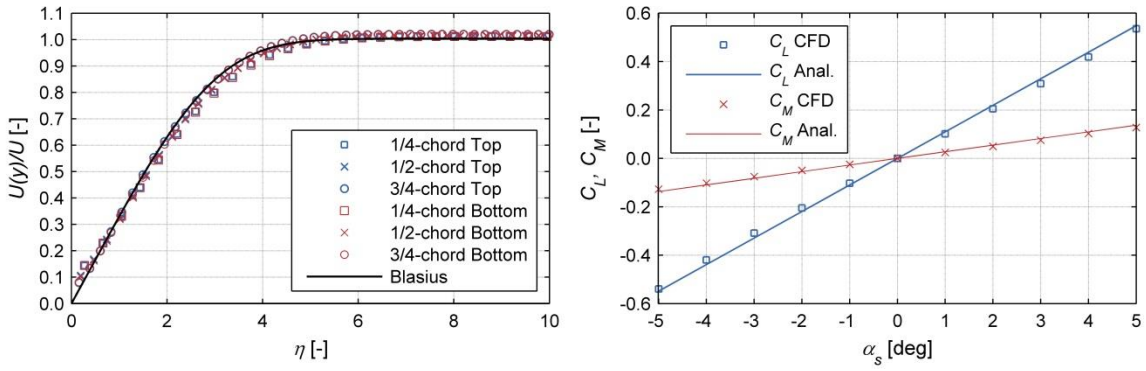

Figure 7: Boundary layer (left) and static wind coefficients (right) for a flat plate.

The advantage of the first approach is that the amplitude of the sinusoidal gust is the actual one to which the section is subjected. With the second approach, the amplitude of the tracked gust might not be the same with the amplitude which is acting on the section as the gust amplitude varies in the along wind direction (cf. Fig. 4). Furthermore, the imaginary part of the admittance is obtained for a gust acting at the stiffness center of the body by using the first approach. The advantage of the second approach is that the influence of the body on the upstream velocity is taken into account, which is neglected by the first approach. Nevertheless, the linear unsteady model (cf. Eqs. (1) and (2)) does not account for this effect, as the tracking location can be arbitrarily far positioned upstream of the leading edge. Hence the influence of the section on the gust is compromised. In experiments, only the second method is applicable.

Figure 9 depicts a time-history of the normalized lift and moment coefficients at $V_r = 16$. The normalized fluctuating lift coefficient is obtained by normalizing the lift coefficient with its derivative and gust amplitude, that is, $\chi_L e^{iKs} = C_L/(C_L' w_0)$, which effectively is a harmonic function factored by the aerodynamic admittance. Similar expression is obtained for the moment. The normalized fluctuating wind coefficients are further compared to the time-histories obtained using the Sears' function. From the figure, it can be observed that the forces sinusoidal. The additional high frequency fluctuations for the CFD model are caused either by the viscous random

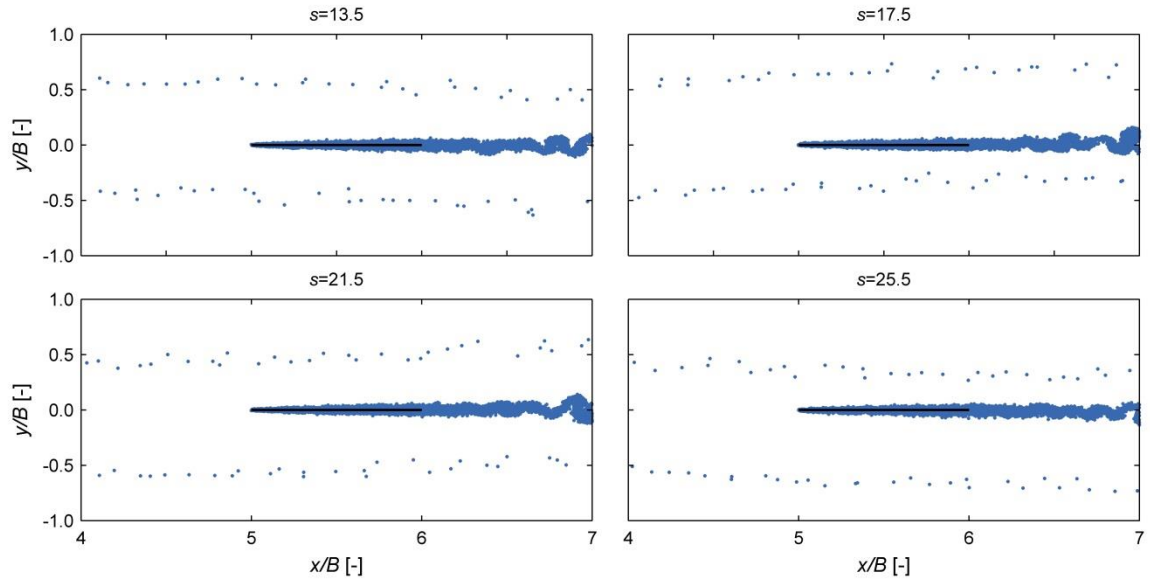

Figure 8: Sequence of particle maps for a sinusoidal gust past a flat plate at $\boldsymbol{V_r = 16}$.

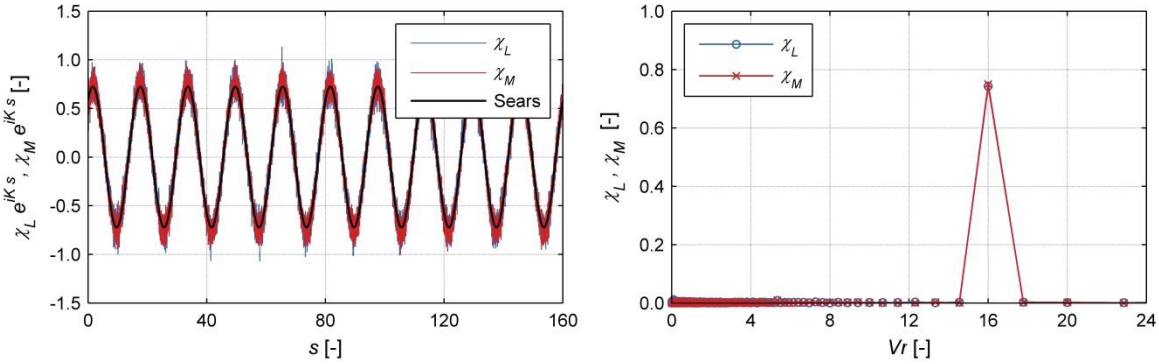

Figure 9: Normalized fluctuating wind coefficients (left) and their FFT for flat plate at $\boldsymbol{V_r = 16}$.

walk or by the vortex-shedding. In fact, Sears' normalized fluctuating coefficient is sort of a least-square fit to the results from the CFD analyses. The FFT of the normalized coefficients (cf. Fig. 9, right) also depicts a clear harmonic in the forces. It is noteworthy to notice that the full expression for the Sears' function is used, obtained as follows (cf. Sears (1941)):

$$\chi = [J_0(k) - iJ_1(k)]C(k) + iJ_1(k), \tag{21}$$

where $C(k)$ is the Theodorsen's function and $J(k)$ is the Bessel function of the first kind.

Figure 10 (left) depicts the real and imaginary parts of the complex aerodynamic admittance obtained using the CFD simulations and the Sears' function. Furthermore, the absolute value of the aerodynamic admittance (cf. Fig 10, right) is given. The admittance is computed for 10 cycles of sinusoidal gust. It is interesting to notice, that in addition to the good correspondence of the absolute values, the separate real and imaginary part correspond well with the Sears' function. As it can be observed from the figure, the gust lags behind the aerodynamic forces for reduced velocities up to $V_r = 8$. Another important particularity is that the aerodynamic admittance of the moment and lift force coincide, which effectively means that the lift force is acting on the 1/4-chord point. A maximum deviation of 10% for the absolute value of the admittance of the CFD model is obtained for $V_r = 2$, while the differences are in the range of $\pm 2\%$ for $V_r > 3$.

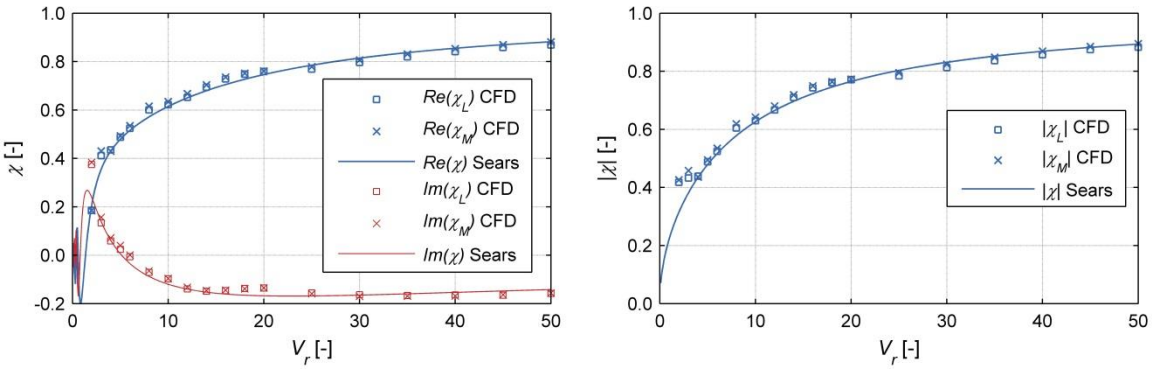

Figure 10: Aerodynamic admittance for a flat plate.

5.2 Experimental validation – 3rd Bosphorus Bridge

Finally, the numerical aerodynamic admittance functions are validated with experimental results for a streamlined bridge deck. The streamlined deck from the 3rd Bosphorus Bridge (also known to as the Yavuz Sultan Selim Bridge) is selected as a reference object with a width of 58.5 m. Static wind coefficients and aerodynamic admittance tests for the reduced velocity range of

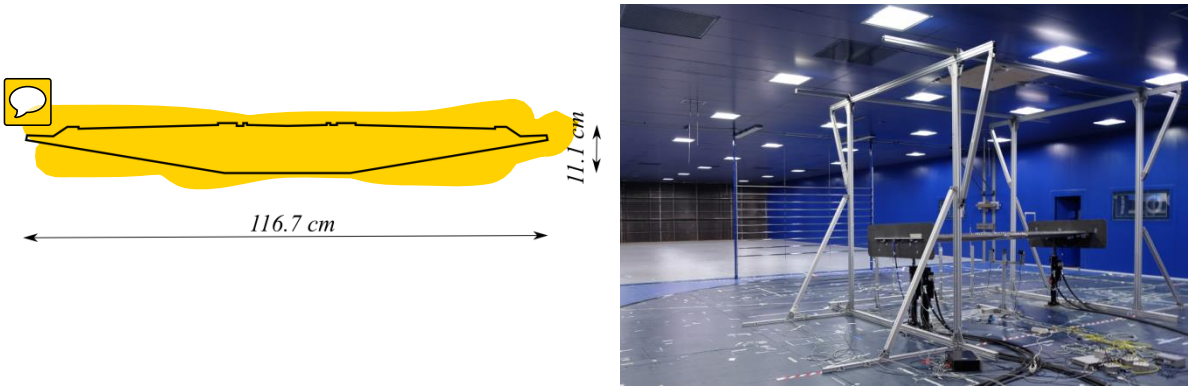

Figure 11: Schematic of the Third Bosphourus Bridge deck model considered in the wind tunnel (left) and the test setup for the aerodynamic admittance tests including ATG (right).

$1.3 \leq V_r \leq 135$ were performed at the Politecnico di Milano boundary layer wind tunnel (cf. Fig 11). A carbon fiber model with a large geometrical scale 1:50, width of 1.17m , height of 0.11 m and length of 3.6 m was built (cf. Fig 11), which was subjected to sinusoidal gust. The sinusoidal gust was generated by an ATG, constituted of ten airfoils with chord of 20 cm, positioned at distance of $6B$ upstream of the section. The Reynolds number varied in the range of $4.9 \times 10^5 \leq Re \leq 1.16 \times 10^6$ and the gust amplitudes in the range of $0.011 \leq w_0/U \leq 0.074$. The model included details such as fences; however, the aerodynamic forces were obtained from the pressure taps positioned on the deck. In total, four rings of pressure taps were positioned along the length of the deck, each ring consisting of 62 taps.

In the CFD simulations, the deck is discretized on 750 panels with a non-dimensional time-step of $\Delta s = 0.0027$ and the Reynolds number amounts to $Re = 7.78 \times 10^5$. The CFD domain was set to accommodate a length of $10B$ behind the leeward edge and approximately $6B$ upstream of the windward edge of the section. Initially, the static wind coefficients are compared to the experimental results. For each angle increment, the lift and moment coefficients are averaged for a minimum time period amounting to $s = 50$. Figure 11 depicts the static wind coefficients, obtained from the CFD simulation and experimental (EXP) tests. A slight overestimation is noted in the lift coefficient for positive angles; while there is an offset in the moment coefficient. Although the aerodynamic forces from the experimental tests are obtained using the pressure taps only on the deck (neglecting the fences and auxiliary equipment), the separation and reattachment point is still influenced by the auxiliary equipment. Taking this into account and the fact that the lift and moment slopes are overestimated by 15% and 10% for the CFD model, respectively, the correspondence is considered to be fair. Figure 13 (left) depicts an instantaneous flow field around the section under laminar freestream.

The aerodynamic admittance using the CFD model is computed for reduced velocity range of $2 \leq V_r \leq 50$, for target gust amplitude of $w_{ct0}/U = 0.035$. Unlike for the flat plate case, the distance between the wakes is taken here as $R = 1.5B$ in order to avoid particles crossing the section. The stiffness center of the deck is position at 6.5B downwind of the particle release location. Figure 13 (right) depicts an instantaneous particle map at the peak of a sinusoidal gust past the bridge deck at $V_r = 16$. Figure 14 depicts the normalized fluctuating wind coefficients for the CFD simulation and experimental tests, at approximately similar reduced velocity, Reynolds number and gust amplitude. In the experiments, it is difficult to obtain exactly the prescribed reduced velocities; hence, the reduced time on the horizontal axis was normalized with the reduced velocity. Good correspondence can be observed, with a slight overestimation by the CFD model, which is probably due to the higher numerical noise due to the viscosity. Figure 15 depicts

the aerodynamic admittance obtained using the CFD model and experimental tests. In case of the experimental results, the sinusoidal gust was recorded using cobra probes positioned at distance *B* upwind of the leading edge for each pressure taps ring. The experimental results depicted Fig. 15 are for the two inner pressure taps rings (R1 and R2), positioned at 40cm in the span-wise direction from both sides of centerline of the experimental model. The inner rings were selected in order to alleviate the end effects of the flow on the model.

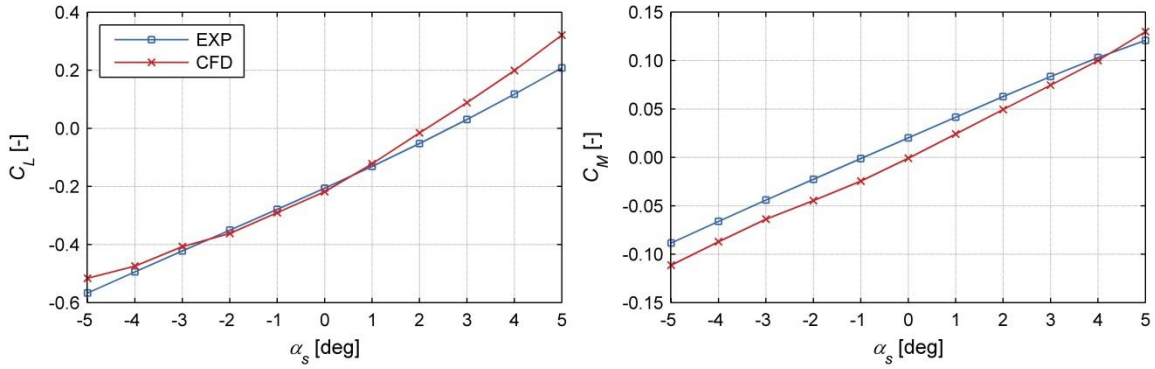

Figure 12: Lift (left) and moment (right) static wind coefficients for the 3rd Bosphorus bridge obtained using CFD simulations and experimental (EXP) tests.

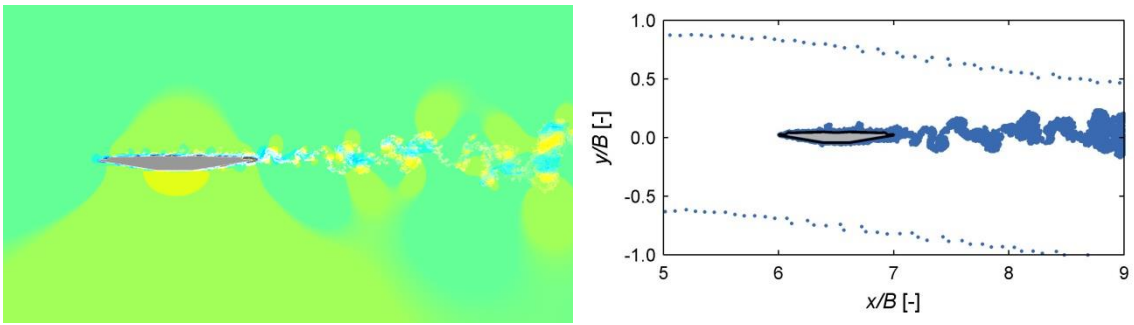

Figure 13: Instantaneous velocity field around the bridge deck under laminar freestream (left) and instantaneous particle map for incoming sinusoidal gust at $\boldsymbol{V_r = 16}$.

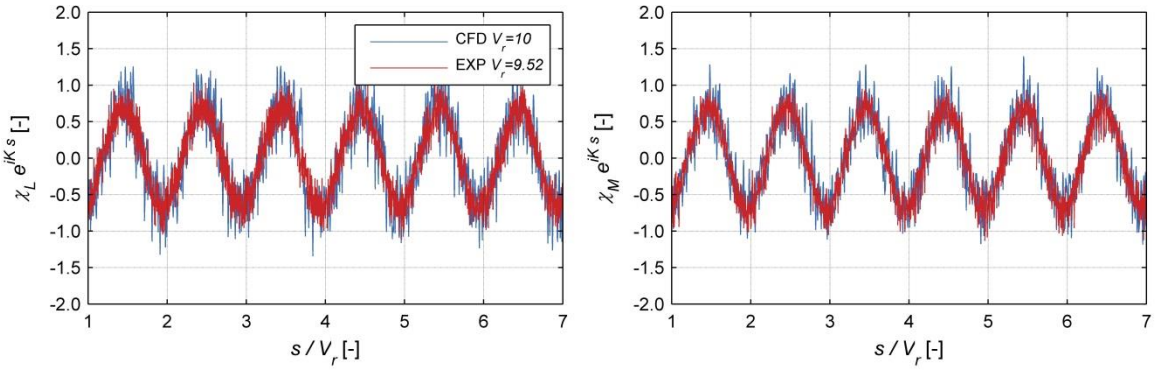

Figure 14: Normalized fluctuating wind coefficients for a bridge deck for the CFD model ($\boldsymbol{Re = 7.78 \times 10^5; w_0/U = 0.040}$*) and the EXP model (*$\boldsymbol{Re = 6.31 \times 10^5; w_0/U = 0.031}$*).*

The aerodynamic admittance for the CFD model is computed by the two approaches, explained in the previous section. In the first case (C1), the sinusoidal gust is tracked down at B upwind of the leading edge, in a similar fashion as for the experimental results. The aerodynamic admittance in

the second case (C2) is computed with a sinusoidal gust tracked at the position of the stiffness center, from a simulation without a section in the CFD domain. For C2, the sinusoidal gust was shifted for $t_{shift} = 1.5B/U$ in order obtain comparable results with the experiments for the imaginary value of the aerodynamic admittance. It is noted that this does not influence the absolute value of the aerodynamic admittance. As it can be observed from the figure, the CFD results are within the range of the experimental results, for both, real and imaginary component. Two reasons seems plausible for difference between C1 and C2 for the CFD model, namely: (i) the distortion of the incoming gust due to the influence of the section and (ii) the variation of the gust amplitude in the along-wind direction. It is noteworthy to notice that in C1, the absolute value of the aerodynamic admittance function tends faster towards unity than in the C2 case. This effect is probably due to reason (i), as the section reduces the incoming gust amplitudes. As discussed previously, the linear unsteady aerodynamic model does not take this effect into account.

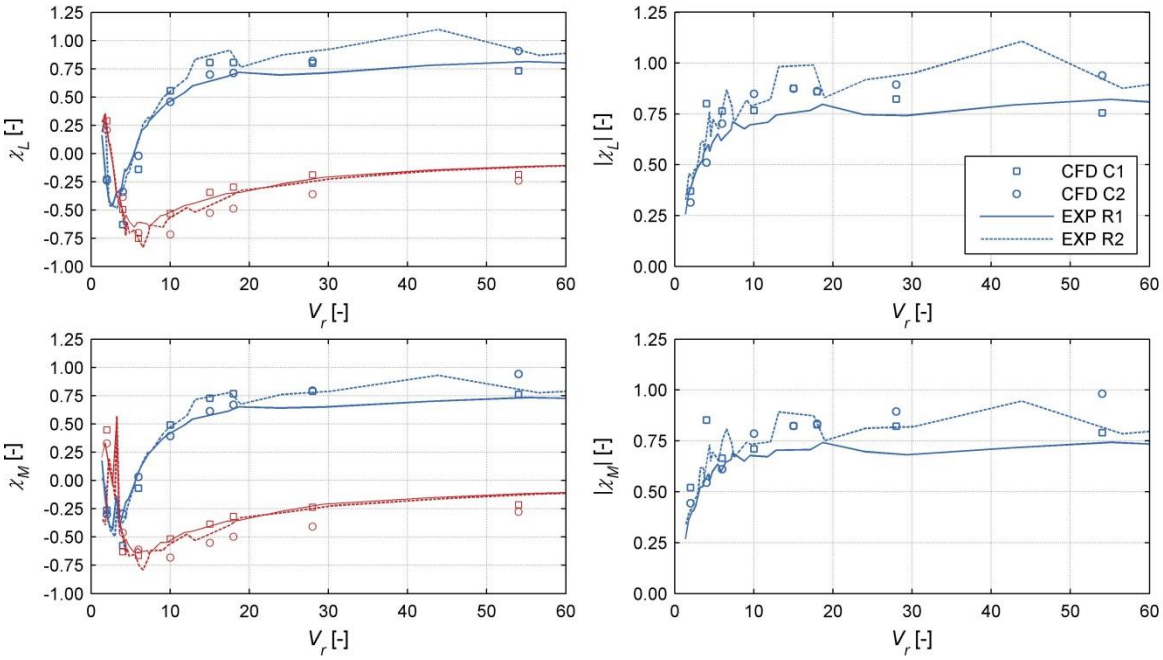

Figure 15: Aerodynamic admittance function of the lift (top) and moment (bottom) force. The real part of the aerodynamic admittance is indicated by blue and the imaginary part by red color (left).

6 SUMMARY AND CONCLUSION

In summary, in this paper we presented a method for determination of the complex aerodynamic admittance based on the VPM. The incoming sinusoidal gust was simulated by modelling the wakes of two fictitious airfoils which are performing in-phase sinusoidal motions. An analytical model for determining the gust amplitudes was extended for direct determination of the released circulation. A flow field investigation was conducted and the behavior of the defined gust quality and gust amplitude was studied within the domain. For the location of interest within the CFD domain, it was shown that the gust is mainly sinusoidal. The aerodynamic admittance was initially verified using Sears' function for a flat plate. Finally, an experimental validation for a bridge deck was conducted, yielding promising results.

In conclusion, the presented method is readily applicable for a numerical determination of the aerodynamic admittance of bridge decks. In future, we intend to extend the current study by conducting parametric investigation on the flow field and by studying the influence of Reynolds number and turbulence intensity on the aerodynamic admittance.

Acknowledgements
IK and GM are grateful to the German Research Foundation (DFG) for providing financial support during IK studies and research stay at the Department of Mechanics at the Politecnico di Milano.

References
Sears, W. (1941). Some aspects of non-stationary airfoil theory and its practical application. J Aero Sci, 8-3, p104-108.
Diana, G., Bruni, S., Cigada, A., Zappa, E. (2002). Complex aerodynamic admittance function role in buffeting response of a bridge deck. J Wind Eng Ind Aerody, 90, p2057-2072.
Diana, G., Rocchi, D., Argentini, T. (2013). An experimental validation of a band superposition model of the aerodynamic forces acting on a multi-box deck sections. J Wind Eng Ind Aerody, 113, p40-58.
Kavrakov, I., Morgenthal, G. (2017). A comparative assessment of aerodynamic models for buffeting and flutter of long-span bridges. Eng, 3, p823-838.
Morgenthal, G. (2002). Aerodynamic analysis of structures using high-resolution vortex particle methods. PhD thesis, Cambridge University.
Stapountzis, H. (1982). An oscillating rig for the generation of sinusoidal flows. Phys E: Sci Instrum, 15, p1173-1176.
Harding, S. F., Bryden, I. G. (2012). Generating controllable velocity fluctuations using twin oscillating hydrofoils. J Fluid Mech 713, p150-158.